

1 Article

2 A Preliminary Analysis of Wind Retrieval, Based on 3 GF-3 Wave Mode Data

4 Lei Wang^{1,2,3}, Bing Han^{1,2,*}, Xinzhe Yuan⁴, Bin Lei^{1,2}, Chibiao Ding^{1,2,3,5}, Yulin Yao⁶, Qi Chen⁶

5 ¹ Key Laboratory of Technology in Geo-Spatial Information Processing and Application Systems, Institute of
6 Electronics, Chinese Academy of Sciences, Beijing 100190, China; wanglei162@mail.ucas.edu.cn (L.W.);
7 leibin@mail.ie.ac.cn (B.L.); cbding@mail.ie.ac.cn (C.D.);

8 ² Institute of Electronics, Chinese Academy of Sciences, Beijing 100190, China;

9 ³ School of Electronic, Electrical and Communication Engineering, University of Chinese Academy of
10 Sciences, Beijing 100049, China

11 ⁴ National Satellite Ocean Application Service, State Oceanic Administration, Beijing 100081, China;
12 harley_yuan@mail.nsoas.org.cn

13 ⁵ National Key Laboratory of Microwave Imaging Technology, Institute of Electronics, Chinese Academy of
14 Sciences, Beijing 100190, China

15 ⁶ China Centre for Resource Satellite Data and Application, Beijing 100094, China; yaoyulin886@163.com
16 (Y.Y.), chenq_cn@163.com (Q.C.);

17 * Correspondence: han_bing@mail.ie.ac.cn; Tel.: +86-10-5888-7208 (ext. 8956)

18 **Abstract:** This paper gives an analysis of measurements of the normalized radar cross-
19 section(NRCS) in Wave Mode for Chinese C-band Gaofen-3(GF-3) synthetic aperture radar (SAR).
20 Based on 2779 images from GF-3 quad-polarization SAR in Wave Mode and collocated wind vectors
21 from ERA-Interim, the feasibility of using ocean surface wind fields and VV-polarized NRCS to
22 perform normalized calibration is verified. The method uses well-validated empirical C-band
23 geophysical model function (CMOD4) to estimate the calibration constant for each beam. In
24 addition, the relationship between cross-pol NRCS and wind vectors is discussed. The cross-pol
25 NRCS increases linearly with wind speed and it is obviously modulated by the wind direction when
26 the wind speed is greater than 8m/s. Furthermore, the properties of the polarization ratio, denoted
27 PR, are also investigated. The PR is dependent on incidence angle and azimuth angle. Two empirical
28 models of the PR are fitted, one as a function of incidence angle only, the other with additional
29 dependence on azimuth angle. Assessments show that the σ_{VV}^0 retrieved from new PR models as
30 well as σ_{HH}^0 is in good agreement with σ_{VV}^0 extracted from SAR images directly.

31 **Keywords:** Gaofen-3; SAR; Wave Mode; calibration constants; cross-pol; noise floor; polarization
32 ratio;
33

34 1. Introduction

35 With the continuous depletion of global petroleum energy, the development and utilization of
36 clean wind energy have become a hot topic in recent decades. Offshore wind energy has been focused
37 by researchers due to the vast area of marine resources. Measurements of offshore wind information
38 also contribute to oil spill monitoring, weather forecasting and understanding of air-sea interactions
39 [1-3]. Spaceborne active microwave scatterometer such as QuickSCAT and ASCAT have provided
40 mature wind products for National Oceanic and Atmospheric Administration(NOAA) [4,5].
41 However, the wind fields acquired by scatterometer cannot be applied to fine scale marine products
42 due to the course spatial resolution (12.5km~25km) [6]. Because of features like imaging at all-
43 weather conditions and high spatial resolution, synthetic aperture radar (SAR) has been widely used
44 in military, economics, and science, and plays an important role in the retrieval of ocean surface wind
45 fields, especially for C-band (~5.3GHz) SAR [7].

46 Numerous studies have revealed that ocean surface normalized radar cross-section (NRCS)
47 obtained from C-band SAR is mainly dominated by resonant Bragg backscattering at the wavelength
48 of centimeter scale [8-10]. This scale roughness is predominantly influenced by local wind and

49 therefore ocean wind information may be extracted from SAR images [11]. In recent decades, several
50 empirical geophysical model functions (GMFs), such as CMOD4 [12], CMOD_IFR2 [13], CMOD5 [14]
51 and CMOD5.N [15] have been proposed to perform ocean surface wind retrieval. These GMFs relate
52 the NRCS to the incidence angle, wind speed at a height of 10m above sea level, and azimuth angle
53 (radar look angle with respect to wind direction). Not only scatterometer, such as QuickSCAT [16,17]
54 and ASCAT [18], they can also accurately retrieve the wind speed from SAR image (within about
55 2m/s), e.g., ENVISAT [19], RADARSAT-1/2 [20-22] and Sentinel-1A/B [23]. However, such GMFs are
56 only suitable for VV-polarized NRCS, no similar models exist to retrieve wind speed from images in
57 HH-polarization. Therefore, it is necessary to convert HH-polarized NRCS to VV-polarization using
58 polarization ratio (PR), denoted as $PR = \sigma_0^{VV} / \sigma_0^{HH}$ [linear units], before retrieving wind speed [24-
59 28]. In traditional research, it is generally believed that the PR is only relevant to incidence angle [24].
60 Recent studies in [27,28] show that the PR is also dependent on speed and azimuth. These results
61 reveal that different satellites have their own optimal PR and GMF. Thus, the choice of suitable hybrid
62 model before retrieving wind fields is critical for Gaofen-3 satellite [29].

63 Recent decades, wind speed retrieval from cross polarized (cross-pol) NRCS has become to a
64 focus due to the saturation of co-pol data at high wind speed. Some studies of cross-pol images have
65 been conducted for RADARSAT-1/2 quad-polarization and dual-polarization [32-37]. Hwang and
66 Zhang et al. [30,31] reveal the breaking contribution of cross-pol NRCS and emphasize advantages of
67 wind retrieval with cross-pol data at high wind speeds. Vachon and Zhang et al. [32,33] propose a
68 cross-pol wind retrieval model which is only relevant to wind speed and independent on incidence
69 angle as well as wind direction, respectively. In [34-36], Hwang and Shen propose that the VH NRCS
70 of RADARSAT-2 dual-polarization mode is also relevant to incidence angle and the noise floor must
71 be considered before wind retrieval. Moreover, Huang et al. [38] conduct an evaluation on cross-pol
72 NRCS in Sentinel-1 IW mode and propose a wind retrieval algorithm related to incidence angle and
73 wind direction. The above studies show that the cross-pol NRCS has potential to retrieve high wind
74 speeds, e.g. hurricanes and typhoons.

75 The accuracy of the retrieved wind vector is strongly affected by the absolute radiometric
76 calibration accuracy of NRCS. Accurate wind speed can be obtained from refined NRCS. Therefore,
77 it is possible to assess the accuracy of the calibration by using GMFs and known wind information.
78 Horstmann et al. [39] propose a method for estimating ERS SAR calibration constant using C-band
79 models and ocean surface wind fields. Stoffelen et al. [40] obtain an accurate calibration of a
80 scatterometer over the ocean using CMOD4 and wind fields from European Centre for Medium-
81 Range Weather Forecasts (ECMWF). This method achieves a calibration accuracy of 0.1 dB. Verspeek
82 et al. [41] propose an estimating correction table based on CMOD5.N to improve ASCAT wind
83 retrieval. Zhu et al. [42] use Numerical Ocean Calibration (NOC) to calibrate HY-2 SCAT and
84 retrieved winds are in good agreement in winds from ECMWF.

85 The Gaofen-3 (GF-3) satellite which was launched on 10 August 2016 by the China Academy of
86 Space Technology (CAST) is the first C-band multi-polarization SAR with the highest resolution of
87 1m in China. It has characteristics such as high resolution, large coverage, long-life operation and
88 multiple imaging modes, including Wave Mode [43]. To date, some preliminary evaluations of ocean
89 application have been carried out. Shao et al. [44] collect 244 Stander Stripmap (SS) and Quad-
90 Polarization Stripmap (QPSI and QPSII) mode images to complete wind and wave retrieval firstly.
91 In [29], Wang et al. validate the GF-3-derived winds against NDBC measurements using SS, QPSI,
92 QPSII, FSI and NSC mode data. Ren et al. [45] conduct a comprehensive analysis of QPSI and QPSII
93 mode data in each polarization. Several empirical algorithms for significant wave height in Wave
94 Mode data and wind retrieval from cross-polarization in typhoons are also discussed in [46,47], which
95 uses GF-3 images acquired in Global Observation (GLO) and Wide ScanSAR (WSC) mode.

96 The remainder of this paper is organized as follows. Section 2 describes the GF-3 Wave Mode
97 SAR images and the other validated data, including ECMWF ERA-Interim re-analysis wind fields
98 and Amazon rainforest images. Methodologies for correcting calibration constants, fitting PR models
99 and cross-pol wind speed retrieval formula are introduced in section 3. Section 4 shows results of

100 calibration, polarization conversion and wind speed retrieval accuracy. Finally, discussion and
101 conclusion are presented in section 5 and 6.

102 2. Description of Datasets

103 2.1. GF-3 SAR Wave Mode images

104 An experiment in [48] shows that GF-3 images can meet the satellites' polarimetric accuracy
105 requirements, and the channel imbalance is 0.5dB as well as a crosstalk accuracy of -35dB. In this
106 study, 6355 GF-3 Level-1A Wave Mode images are collected between March 1, 2017 and December
107 31, 2017 over the Pacific, Atlantic and Indian Ocean. The task of Wave Mode is to observe ocean
108 surface waves over open ocean, and the size of Wave Mode image is about 5km × 5km every 50 km
109 along the orbit. Incidence angle is the predominant difference between Wave Mode and other modes.
110 Although the incidence angle of Wave Mode ranges from 20° to 50°, it only fixes in 28 beams with a
111 narrow data acquisition window about 0.4°. This results in discrete incidence angle for images
112 between different beams, e.g. incidence angle of beam 189 is about $21.5 \pm 0.2^\circ$ and the incidence
113 angle of beam 190 is about $23.7 \pm 0.2^\circ$ etc. [46,43]. The parameter details of Wave Mode products
114 are listed in Table 1 and the time distribution of data in each ocean is listed in Table 2.
115

116 **Table 1.** Parameters for GF-3 Wave Mode.

Imaging mode	Incidence angle (°)	Polarization	Resolution (m)	Swath (km)
WAV	20-50	HH+VV+HV+VH	10	5

118 **Table 2.** Time Distribution of SAR Images in Each Ocean

Oceans	Pacific	Atlantic	Indian
Distribution	Mar, Apr, Sep, Oct, Nov, Dec	Apr, May, Jun	Mar, April

121 The Level-1A products are single look complex (SLC) images. Let I represents real channel of
122 images, Q as the imaginary channel. The equation of NRCS is as follow.
123

$$124 \quad \sigma^0 = 10 * \log \left[\left(\frac{I}{32767} * Qualify \right)^2 + \left(\frac{Q}{32767} * Qualify \right)^2 \right] - K_const \quad (1)$$

125 Where σ^0 is the NRCS in dB, Qualify is the QualifyValue in product description xml of GF-3, and
126 K_const is the calibration constant.

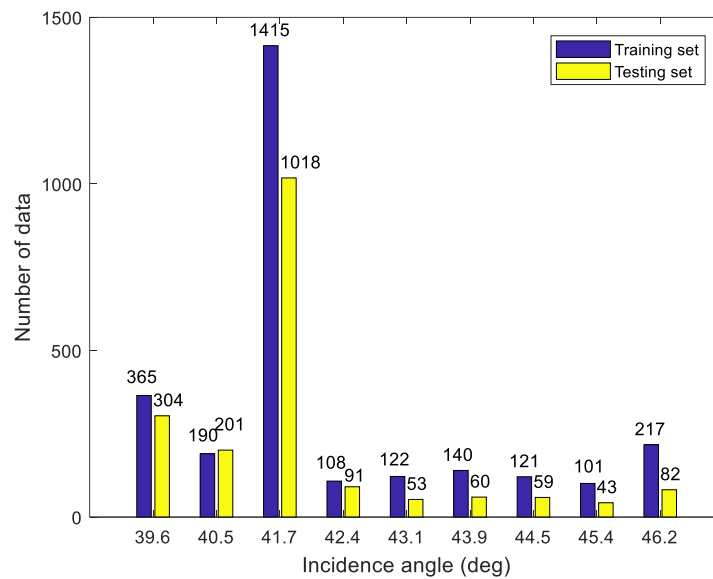
127 Several studies indicate that wind speed can only be retrieved from pure ocean SAR images
128 which are free of sea features not due to the local wind, e.g. ice and slicks [2,49]. To screen out the
129 Wave Mode images which are not affected by features due to slicks or ocean phenomenon, the
130 homogeneity check procedure proposed in [46] is used before the experimental study. Wang et al.
131 [46] show that the Wave Mode normalized variance ($cvar_vv$) computed from VV-polarization images
132 can be used as a standard for verifying image homogeneity. Here, we also choose the images which
133 with $1.1 < cvar_vv < 1.6$ for developing and validating wind retrieval algorithms. The parameter
134 of homogeneity test is defined as

$$135 \quad cvar_vv = var \left(\frac{I - \bar{I}}{\bar{I}} \right) \quad (2)$$

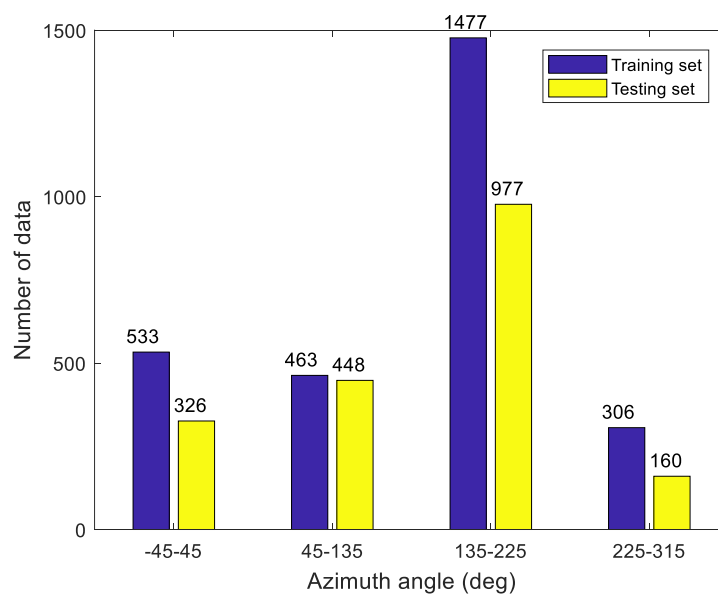
136 where \bar{I} is the mean intensity of GF-3 Wave Mode image in VV-polarization. In addition,
137 inappropriate receiver gain setting causes too high energy input to the ADC converter and may lead
138 to saturation of output power [49]. It greatly affects the experimental results. Hence, this experiment
139 only selects SAR images with 0% saturation coefficient which is provided in product description xml.

140 After the above two preprocessing processes, a total of 4690 GF-3 Wave Mode images are
141 selected from 6355 images. The result shows that the small incidence angle (in-angle < 36°) co-pol
142 data is almost saturated for the 10 months in 2017, according to product description xml. Therefore,
143 the analyzed incidence angle of this paper is only from 39° to 47°. The detail information of data
144 distribution is shown in the Figures 1-3 below. To guarantee the validity of experiment, this

145 experiment divides the whole data into training and testing set randomly first. Then, a small amount
 146 of data is adjusted artificially so that both sets can cover full range of incidence angles, azimuth angles
 147 and wind speeds. Finally, 2779 match-ups are chosen as training set and other 1911 samples as testing
 148 set.



149 **Figure 1.** Incidence angle histogram of the data set



153 **Figure 2.** Azimuth angle histogram of the data set

150
151
152

154
155
156

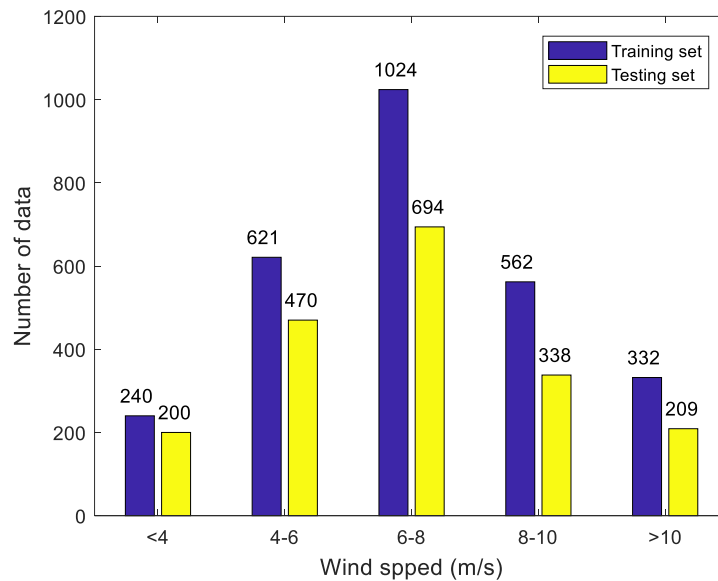


Figure 3. Wind speed histogram of the data set

157
158
159

160 2.2. Other Validation Sources

161 ERA-Interim is a global atmospheric re-analysis from 1979, continuously updated in real time,
162 provided by ECMWF which is an independent intergovernmental organization supported by 34
163 states. The re-analysis wind field data is widely used in retrieval and comparison of wind vectors [12-
164 15]. In this study, the spatial resolution of wind products downloaded on [50] is $0.125^\circ \times 0.125^\circ$
165 (lat/lon), and the temporal resolution is 6h (00:00, 06:00, 12:00, 18:00).

166 The Amazon rainforest has excellent temporal and spatial stability as a radar distributed target
167 calibration source. And its maximum backscatter deviation is about 0.2dB [51]. There have been
168 numerous researches using the Amazon rainforest for radar radiometric calibration [52]. Here, this
169 experiment uses beam 205 SAR images which have a large number of data and corresponding beam
170 of the Amazon rain forest Wave Mode SAR images to validate the feasibility of ocean calibration.

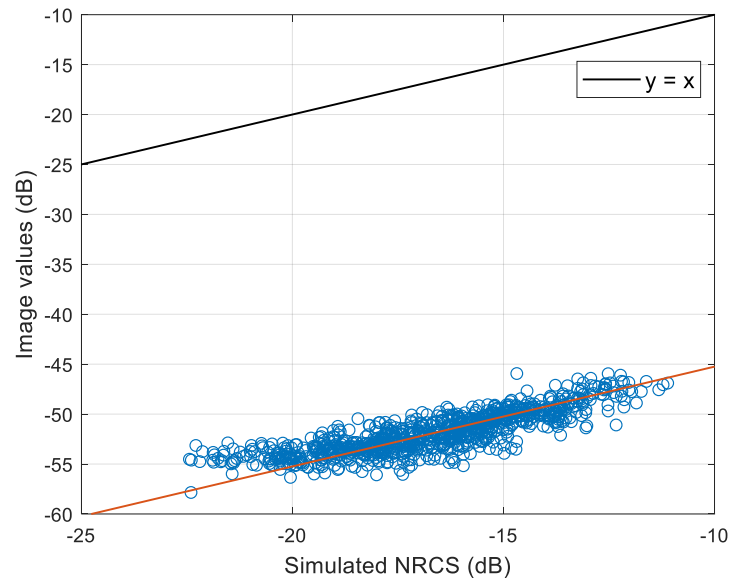
171 3. Experiments and Analysis

172 For the 2779 training data and 1911 testing data, a 512×512 pixel boxcar is used in each center
173 of Wave Mode images to average the NRCS in co-polarization (HH and VV), so that the NRCS
174 spacing is about 5km. As mentioned in section 2, the wind fields' spatial resolution as about $12.5\text{km} \times$
175 12.5km . To improve the match accuracy between wind fields and SAR images, we interpolate the
176 wind field time to 1h using a cubic spline interpolation and use bilinear interpolation to interpolate
177 four velocity components near the center point to the center. And the time difference between SAR
178 image and wind vector is within 30min.

179 3.1. Calibration Method Based on Ocean Wind

180 As shown in equation (1), the NRCS in dB is linear with the calibration constant. It provides a
181 possibility for using the wind fields and GMFs to retrieve the calibration constant. In [53], it is found
182 that CMOD4 has a better performance than CMOD5 under low to moderate wind speed. The wind
183 speed range used in this paper is mainly focused on low to moderate wind speeds. Therefore, this
184 experiment uses CMOD4 to obtain simulated VV-polarized NRCS. The difference between simulated
185 NRCS and the value extracted from the corresponding image directly is the stimulated calibration
186 constant. This method requires plentiful fitted data to ensure the accuracy of results and each beam
187 has their own calibration constant. Therefore, the match-up data of 41.7° incidence angle (beam 205)
188 in the training set is used to verify the calibration method. To guarantee the reliability of the

189 calibration method, this experiment only selects data with wind speed higher than 4m/s [39].
 190 Moreover, the distribution of wind speed and direction in the experimental data set also affects the
 191 calculation of calibration constant. Hence, we first split the training set into wind speed bins of size
 192 2m/s and azimuth bins of size 90°. Then, let each speed bin has roughly the same amount of data and
 193 filter data in each speed bin so that the distribution of azimuth angle is uniform. Finally, 901 uniform
 194 match-ups are obtained to implement the calibration method. Figure 4 shows the relationship
 195 between simulated NRCS by CMOD4 and values obtained directly from VV polarized images.



196
 197
 198 **Figure 4.** Relationship between simulated NRCS and values obtained directly from images
 199

200 The solid black line in Figure 4 is the bisector of the axis quadrant and the solid red line is the
 201 fitting curve of the training data with the same slope. As shown in the Figure, the difference between
 202 the simulated NRCS and image values is a constant. The best calibration constant is calculated using
 203 a minimum squared-error criterion. And the calibration constant calculated is 29.486. The calibration
 204 constant of beam 205 provided by China Centre for Resources Satellite Data and Application is 29.665.
 205 The difference between provided constant and calculated constant is within 0.2dB. It shows the
 206 method has a good performance. The obtained calibration constants of each beam are listed in
 207 appendix A.

208 3.2. Analysis of Wind sensitivity for Cross-pol NRCS

209 The cross-pol backscattering signal-to-noise ratio (SNR) of ocean surface is much weaker than
 210 co-pol signal. Therefore, it is necessary to compare cross-pol NRCS with the system noise floor before
 211 wind retrieval [36]. The Institute of Electronics, Chinese Academy of Sciences provides a ground
 212 system processing technology for GF-3 satellite and is able to obtain the noise gain coefficient of Wave
 213 Mode. Due to the limited number of products with system noise gain coefficient, only 138 sets of
 214 beam 205 match-ups with noise floor are collected. Figures 5 (a) and (b) show the HV-polarized NRCS
 215 as a function of ERA-Interim re-analysis wind speed and the difference between σ_{HV}^0 and σ_{HV}^0
 216 which is removed noise floor, respectively.

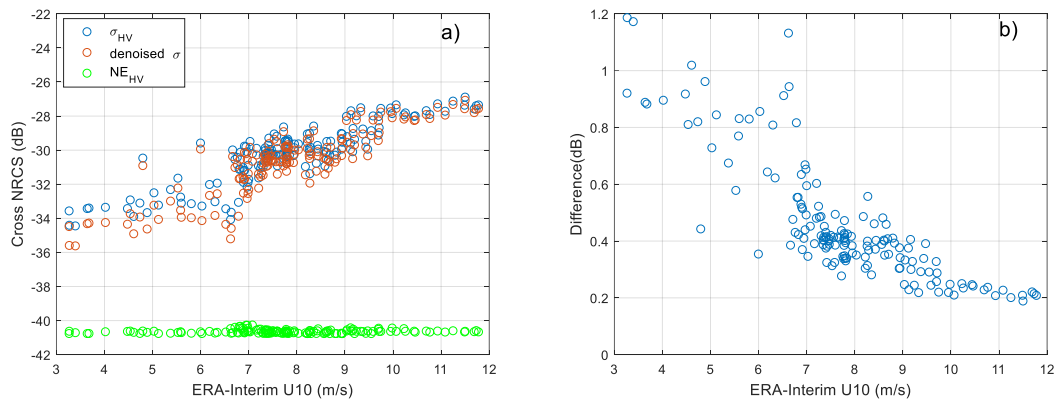
217 As illustrated in Figure 5 (a), the HV-polarized noise floor of beam 205 is about -40 dB. It is
 218 sufficiently low and the noise performance of GF-3 Wave Mode is better than RADARSAT-2 quad-
 219 polarization mode which has the noise floor of -36 dB [45]. Figure 5 (b) shows that the noise floor has
 220 a some effect on cross-pol signals at low wind speed (< 10 m/s) and the difference between σ_{HV}^0 and
 221 denoised σ_{HV}^0 can be ignored at high wind speed. However, the number and distribution of noise
 222 floor is limited in this experiment. The noise floor of different beams may have some differences and
 223 σ_{HV}^0 without noise removed also shows a clear linear relationship with wind speed. Therefore, this

224 experiment temporarily ignores the effect of noise floor. The relationship between the NRCS σ_{HV}^0
 225 after calibration correction and wind speed is shown in Figure 6. Different colors represent different
 226 incidence angles. As shown in Figure 6, the σ_{HV}^0 is independent on incidence angle and exists
 227 obvious linear relationship with wind speed. The black solid line is obtained using a non-linear least-
 228 squares method, and the formulation is

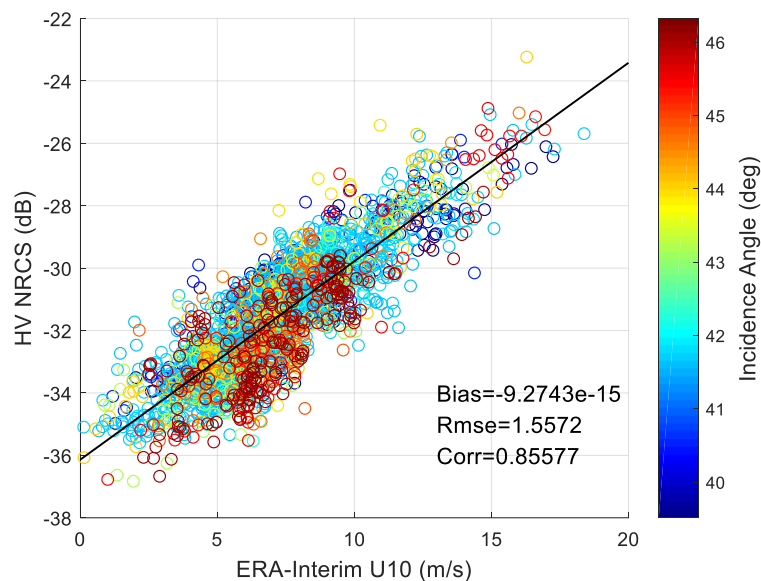
$$229 \quad \sigma_{HV}^0 = 0.6359 * U_{10} - 36.1384 \quad (3)$$

230 where σ_{HV}^0 is the HV-polarized NRCS in dB and U_{10} is the wind speed at 10m.

231

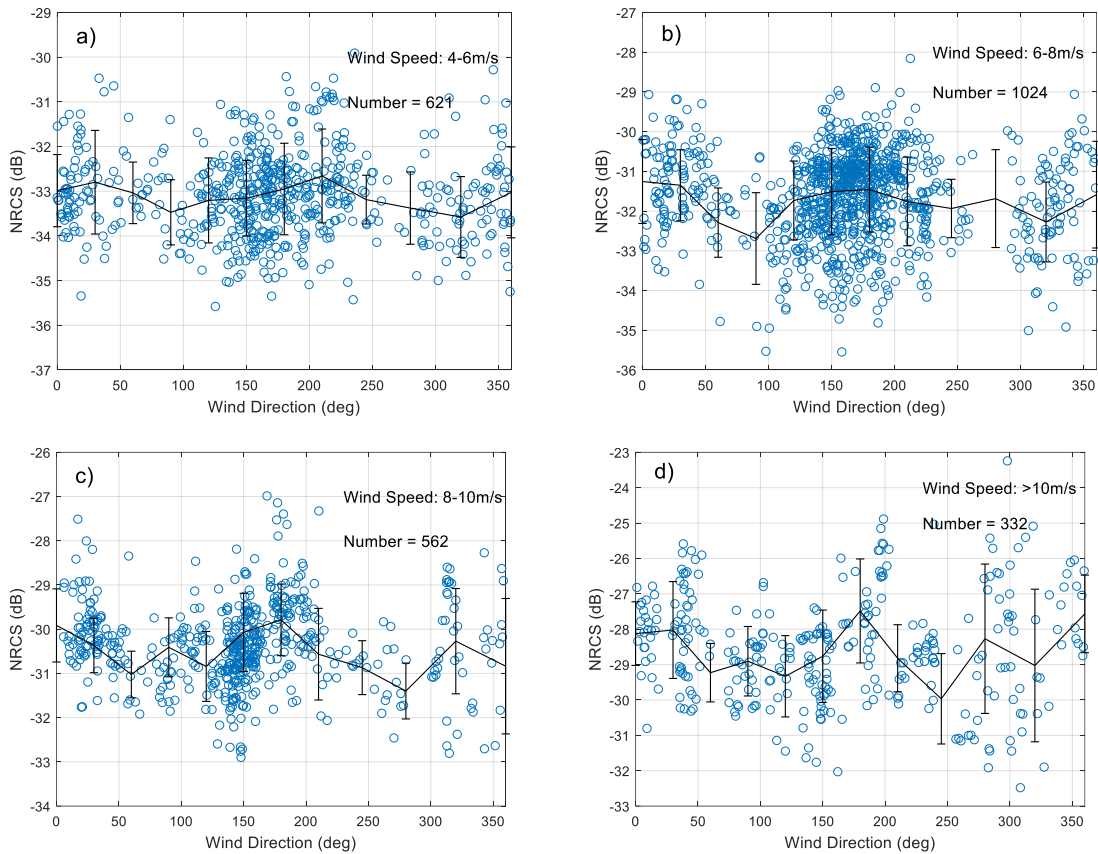


232
233
234
235
Figure 5. HV-polarized NRCS and noise floor versus wind speed



236
237
238
239
240
241
242
243
244
Figure 6. Relationship between NRCS and wind speed (different colors represent different incidence angle)

240 The wind retrieval algorithm of cross-pol NRCS in this study is similar to the formula in
 241 [32,33,45]. The retrieved wind speed using (3) has an RMSE of 1.56 m/s and a correlation coefficient
 242 of 0.86. It indicates the accuracy of cross-pol wind retrieval algorithm under low to moderate
 243 wind speed, and wind speed can be retrieved from cross-pol NRCS directly without inputting wind
 244 direction and incidence angle.



245

246

247

248

249

250

251

252

253

254

255

256

257

Figure 7. Relationship between cross-pol NRCS and azimuth angle

This paper also assessed the relationship between cross-pol NRCS and azimuth angle at different winds. The training set is divided into 4-6m/s, 6-8m/s, 8-10m/s, >10m/s four sets, respectively, according to wind speed, and the variation trend of σ_{HV}^0 with azimuth angle is shown in Figures 7(a)-(d). Figures 7 also draw the mean value line at each bin 30° with errorbars. When speed is higher than 8m/s, the σ_{HV}^0 is subject to obvious wind direction modulation and the maximum change is about 2.5dB in different wind directions. This property is consistent with GF-3 QPSI and QPSII mode data in [45]. Therefore, the influence of wind direction should be considered when retrieving high wind speeds, e.g. hurricanes and typhoons.

258

3.3. Development of PR Models

259

260

261

262

263

Figure 8 shows the relationship between PR and incidence angle as well as wind speed based on 2779 training data. Different colors represent the different wind speeds. And the errorbar of each incidence angle bin is also plotted. The PR rises rapidly with increasing incidence angle as previous reported.

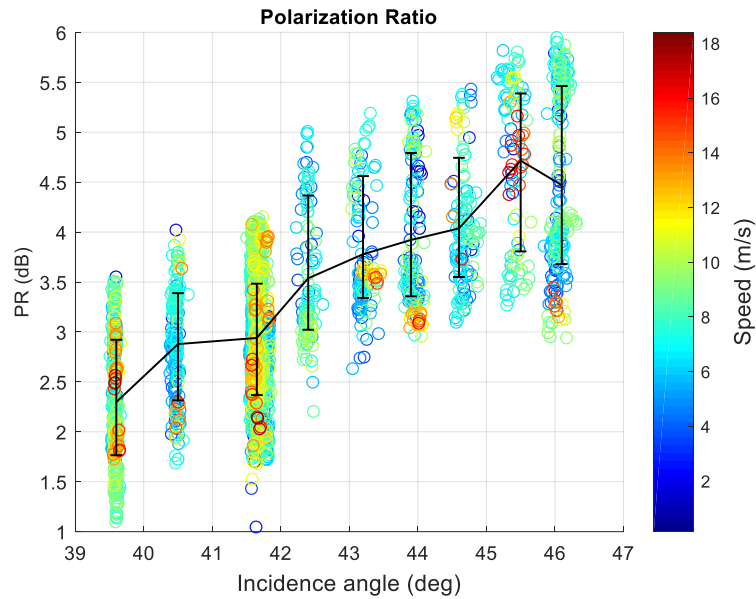


Figure 8. PR as a function of incidence angle (different colors represent different wind speed)

Here, A PR mode which is only related to the incidence angle is first fitted and define it as Model 1. The formulation is

$$PR = Aexp(B\theta) + C \tag{3}$$

where PR is in linear unit, and A, B as well as C are coefficients fitted by a nonlinear least squares method given in Table 3.

Table 3. Coefficients of Model 1

Coefficient	Fitted values
A	0.02985
B	0.09727
C	0.305

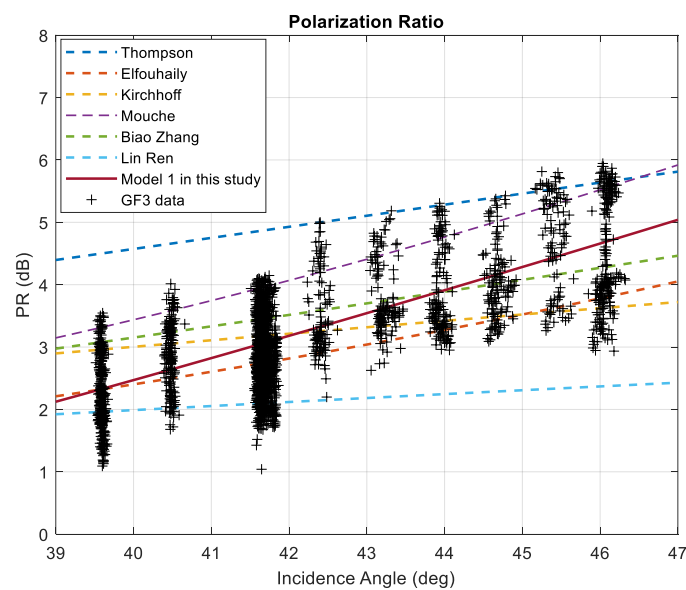


Figure 9. Comparison between Model1 and other PR models

264
265
266
267
268
269
270
271
272
273
274
275

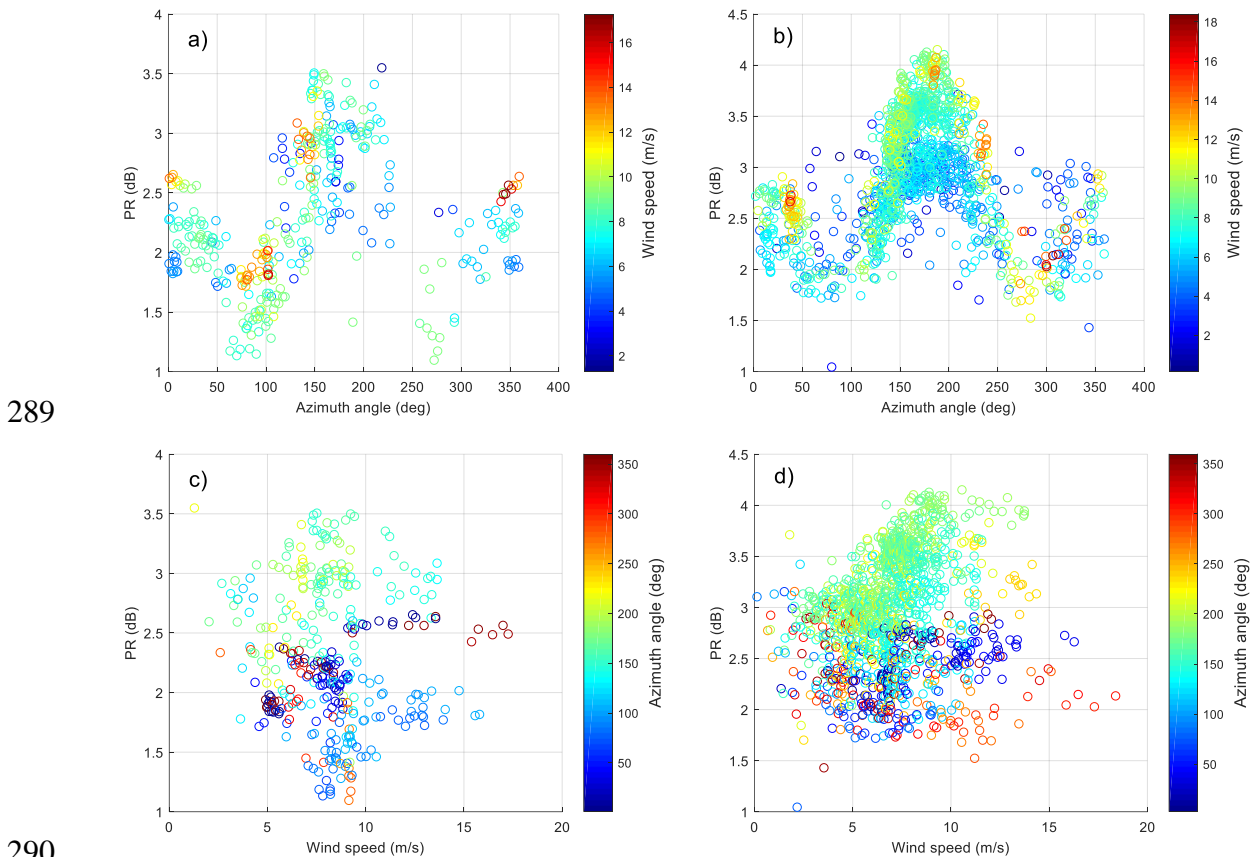
276

277
278
279
280

281 Comparison with other PR models introduced in section 1 is shown in Figure 9. PR models of
 282 Biao Zhang and Mouche [27,28] are also an exponential of the incidence angle like the one in present
 283 study, however different coefficients are found. The formulation of other researchers [24,45] is
 284 expressed as PR

$$285 \quad PR = (1 + 2\tan^2\theta)^2 / (1 + \alpha\tan^2\theta)^2 \quad (4)$$

286 where α is an adjustable parameter. As illustrated in Figure 9, the Model 1 is closest to the mean of
 287 GF-3 Wave Mode.
 288



289

290

291

292 **Figure 10.** (a) and (b) represent the variation between PR and azimuth angle and different color shows different
 293 wind speed. (c) and (d) show the relationship between PR and wind speed. Different color represents different
 294 azimuth. (a) and (c) are at incidence angle 39.6° . (b) and (d) are at incidence angle 41.6° .

295

296

297 To give a more comprehensive PR analysis for GF-3 Wave Mode data, the relationship between
 298 PR and azimuth angle is also studied. It shows a similar characteristic as in [28]. The variation of PR
 299 with azimuth angle and wind speed is shown in Figures 10 (a), (b), (c) and (d) at the incidence angle
 300 of 39.6° and 41.7° (beam 202 and 205), respectively. Figures 10 (a) and (b) show that there is an
 301 approximate cosine relationship between PR and azimuth angle like the characteristic between NRCS
 302 and azimuth angle. The maximum of PR is observed in downwind direction ($\phi = 180^\circ$), a secondary
 303 maximum is appeared in upwind direction ($\phi = 0^\circ$) and the minimum values are in crosswind ($\phi =$
 304 90°). This is slightly different from NRCS which appears maximum in upwind and secondary
 305 maximum value in downwind. In addition, Figures 10 (c) and (d) show the PR tends to increase with
 306 the increase of wind speed ($<10\text{m/s}$) in the downwind, while it is independent with wind speed in
 307 other wind direction. However, it cannot be concluded that the PR increases linearly with wind speed
 308 in the downwind due to insufficient high wind speed data in downwind. Hence, this experiment
 309 temporarily ignores the influence of wind speed and fit training set using nonlinear least squares,
 310 deriving Model 2 for PR with additional dependence on azimuth angle. The Model 2 is assumed to follow

$$PR(\theta, \phi) = C_0(\theta) + C_1(\theta) \cos \phi + C_2(\theta) \cos 2\phi \quad (5)$$

where ϕ is azimuth angle and the PR is in linear unit. In each azimuth angle, the relationship between PR and incidence angle is also defined as exponential function.

$$PR_\phi(\theta) = A_\phi \exp(B_\phi \theta) + C_\phi \quad (6)$$

The coefficients C_i ($i = 0, 1, 2$) can be calculated by the method of undetermined coefficients, and the formulas are as follow

$$C_0(\theta) = (PR(\theta, 0) + PR(\theta, \pi) + 2PR(\theta, \pi/2))/4 \quad (7a)$$

$$C_1(\theta) = (PR(\theta, 0) - PR(\theta, \pi))/2 \quad (7b)$$

$$C_2(\theta) = (PR(\theta, 0) + PR(\theta, \pi) - 2PR(\theta, \pi/2))/4 \quad (7c)$$

First, the coefficients (A_ϕ , B_ϕ , C_ϕ) of three main directions (upwind, downwind, crosswind) are fitted using a nonlinear least squares method. Then using them to obtain coefficients C_i . Table 4 shows the fitting results.

Table 4. Coefficients of Model 2

Coefficients	Fitted values
A_0	0.1715
B_0	0.06242
C_0	-0.4342
$A_{\pi/2}$	0.9331
$B_{\pi/2}$	0.03606
$C_{\pi/2}$	-2.44
A_π	0.000393
B_π	0.1912
C_π	1.119

4. Validation and Results

4.1. Results of Ocean Calibration

The calibration constant provided by China Centre for Resources Satellite Data and Application is derived from system bandwidth and antenna pattern and has not been verified by field calibration. Therefore, 7 GF-3 Wave Mode SAR images of the Amazon rainforest area in beam 205 are collected to verify the calibration constant obtained in section 3.2. The distribution of Amazon rainforest γ is shown in Figure 11.

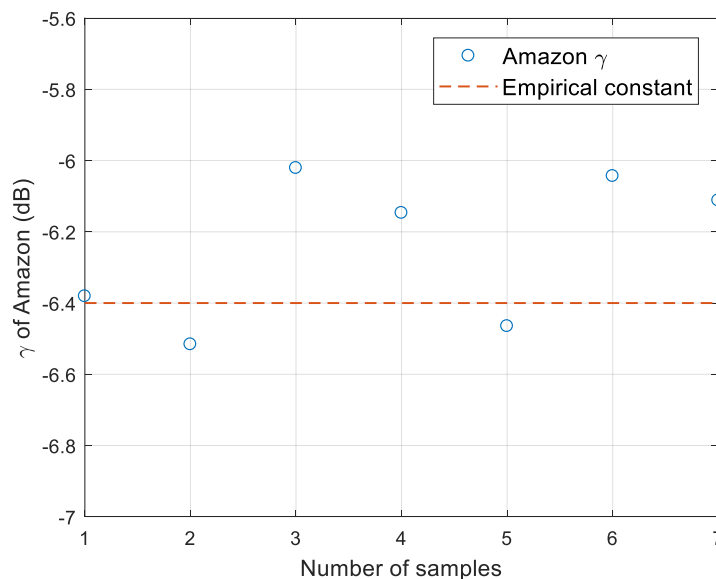


Figure 11. Distribution of Amazon rainforest γ

336

337

As described in [52], the γ of Amazon rainforest can be considered as a constant value due to the stability of this area and it is independent on incidence angle. The γ can be characterized as

338

$$\gamma = \sigma^0 / \cos \theta = \beta^0 \tan \theta \quad (8)$$

339

340

where γ describes the reflectivity of distributed scatterers per unit area of the incident wave front,

341

σ^0 describes the reflectivity per unit area of horizontal surface and β^0 describes the radar reflectivity per unit pixel area [54]. It is generally accepted that the γ of Amazon rainforest is around

342

$-6.47 \pm 0.71 dB$ according to [52]. Figure 11 illustrates the γ of GF-3 Wave Mode data in beam 205 is around $-6.4 \pm 0.4 dB$. Therefore, it can

343

be demonstrated that the calibration constant obtained using the ocean calibration is accurate. And if

344

enough data can be acquired, the calibration constant can be obtained continuously using the ocean

345

surface wind fields, which provides the possibility for normalized calibration.

346

347

Based on the obtained calibration constant, this experiment uses GMFs to complete wind speed

348

retrieval on beam 205 data of testing set. Figures 12 (a)-(d) show the comparison between ERA-

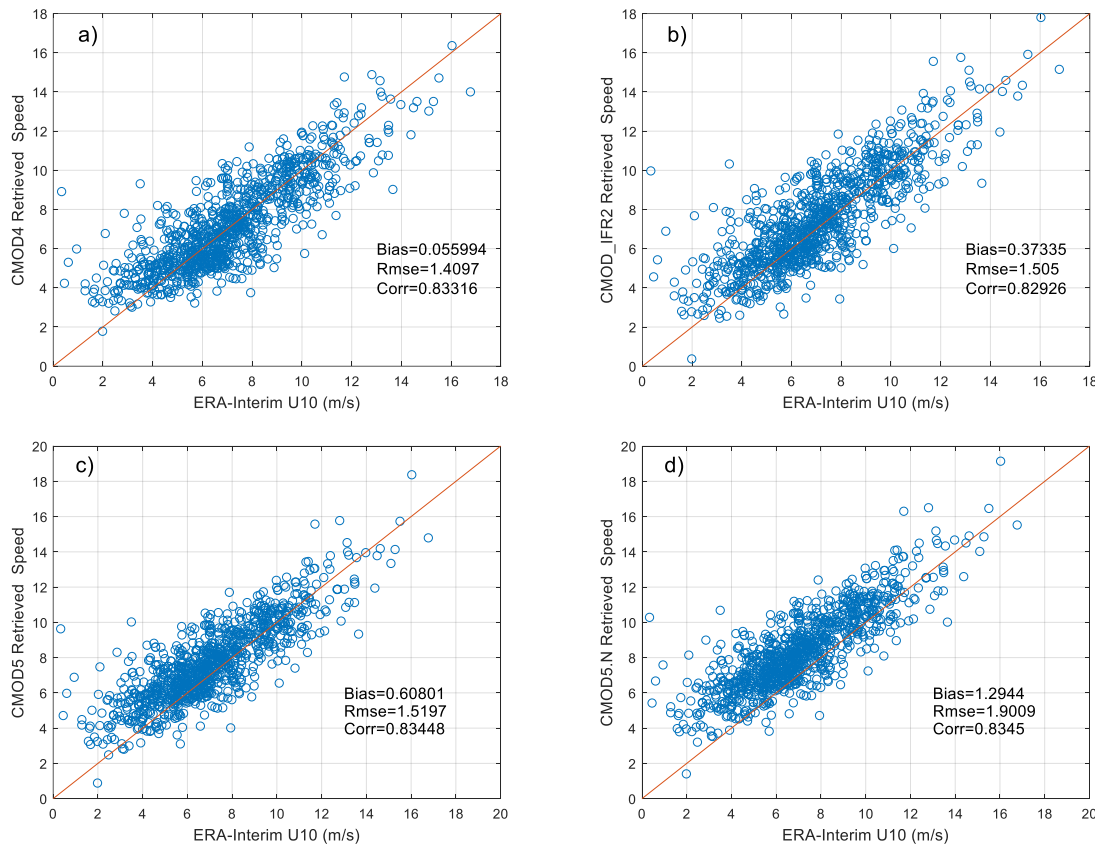
349

Interim wind speeds and retrieved wind speeds using CMOD4, CMOD_IFR2, CMOD5, CMOD5.N ,

350

respectively.

351



352

Figure 12. Comparison of ERA-Interim U10 with SAR-derived wind speeds

353

354

355

356

357

As demonstrated in Figures 12, the estimated calibration constant can be well applied to SAR

358

image wind speed retrieval and the RMSE of retrieved speed is less than 2m/s. However, large

359

inaccuracies may occur in wind retrieval using GMFs when the wind speed is lower than 2m/s. The

360

accuracy of retrieved speed using CMOD4 is higher than others at low to moderate wind speeds and

361

its RMSE is 1.41m/s. The advantage of CMOD5 cannot be verified due to the lack of data when the

362

wind speed comes to high.

363

4.2. Validation of Wind Retrieval for Cross-polarization

364 The testing set is used to evaluate the performance of cross-polarization wind retrieval formula
 365 in this paper compared with algorithms in [32,33,45]. The RMSE, bias and R-squares between ERA-
 366 Interim U10 and retrieved speed is listed in Table 5.
 367

368
 369

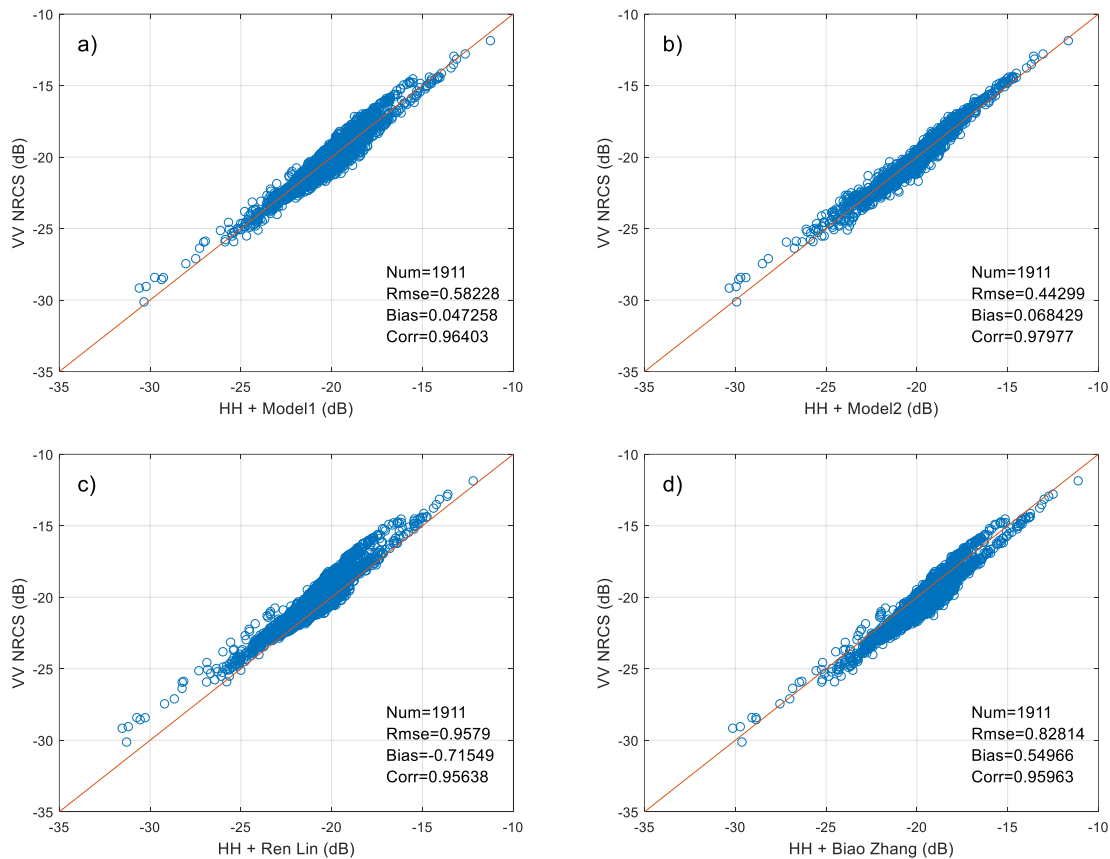
Table 5. Comparison of Wind Speed Retrieval Algorithm

	Rmse (m/s)	Bias (m/s)	R-squares
Mine	1.4990	-0.1605	0.6310
Vachon	1.6043	0.2191	0.5773
Zhang	1.6227	-0.0106	0.5675
Ren	2.0371	-1.1586	0.3184

370
 371
 372
 373
 374

As shown in Table 5, the algorithm fitted in this paper has the optimal inversion accuracy with RMSE 1.5 m/s. The formula proposed by Zhang has the smallest bias with -0.027 m/s. The retrieval result is slightly poor when the formula fitted by QPSI and QPSII data is applied to the Wave Mode data, which has RMSE with 2.04 m/s and bias with -1.16 m/s.

375 4.3. Validation of PR Models using Testing Set



376

Figure 13. Comparison of four different PR models based on testing set

377
 378
 379
 380
 381
 382
 383

To evaluate the performance of two fitted PR models, we test the models in testing set and compare two models with different models in [27,45]. PR model proposed by Zhang in [27] is a function of incidence angle as well as wind speed and model fitted by Ren in [45] is dedicated to GF-3 QPSI and QPSII mode data.

384 Figures 13(a)-(d) illustrate the comparison of four PR models. The abscissa of figure is retrieved
 385 NRCS by PR model and the ordinate is NRCS from SAR image in VV polarization. Figures 13 also
 386 show the root-mean-square error (RMSE), bias and correlation coefficient for each model. It is shown
 387 that two models used in this study are in better agreement with Wave Mode data. The bias of Model1

388 and Model2 is much lower than two other models. And Model 2 which considers the influence of
389 wind direction has a smaller RMSE (0.443dB) and larger correlation coefficient (0.98). In addition,
390 Figure 13(c) shows the PR model proposed for GF-3 QPSI and QPSII mode cannot be well used in
391 Wave Mode data. The retrieved NRCS is generally lower than observation. There may be two reasons
392 for this result. First, the imaging bandwidth and system noise floor of two operating modes are
393 different. These may affect the observation of NRCS. In addition, the PR model in Figure 13(c) is
394 mainly fitted by data with incidence angles between 35°-38°, while PR models in this study are mainly
395 applicable to data with incidence angles greater than 39°, due to the lack of small incidence data.

396 5. Discussion

397 In this paper, we conduct a preliminary analysis of SAR images in Wave Mode for GF-3 satellite.
398 2779 GF-3 Wave Mode NRCS and wind vectors for the corresponding location are collected as
399 training set and additional 1911 match-ups are as testing set. To reduce the effect of speckle noise and
400 improve the matching precision of the data set, the SAR NRCS is first sampled from 10m pixel spacing
401 to 5km firstly, then the wind field interval is interpolated to 1h and the wind vectors of the center of
402 each SAR image is calculated using bilinear interpolation.

403 A simple method for absolute radiometric calibration using ocean surface wind fields and
404 CMOD4 is introduced and tested. Due to the linear relationship between NRCS and calibration
405 constant, an estimator of calibration constant can be obtained by calculating the difference between
406 the simulated NRCS and image value. Since the calibration constant given by China Centre for
407 Resources Satellite Data and Application is only calculated by combing system bandwidth and
408 antenna pattern, this experiment also verifies the constant using Amazon rainforest data. The result
409 shows the obtained Amazon rainforest γ using estimated calibration constant is in good agreement
410 with empirical γ . This normalized calibration method provides a more convenient and affordable
411 way for future absolute radiometric calibration. It saves the expensive cost of calibration using corner
412 reflector and can obtain an accurate calibration constant continuously.

413 The relationship between cross-pol images of Wave Mode and system noise floor, wind vectors
414 and satellite geometry parameters are also investigated. The experiment indicates that the system
415 noise floor of cross polarization is about -40dB. It is low enough and stable. There is a clear linear
416 relationship between cross-pol NRCS and wind speeds in the case of ignoring noise floor effects, and
417 the cross-pol NRCS is independent on incidence angle. As the wind speed increase, the cross-pol
418 NRCS is more affected by azimuth angle. Therefore, it is necessary to consider the azimuth angle
419 when retrieving high wind speed in the future.

420 The PR of Wave Mode is not only dependent on incidence angle but also modulated by the
421 azimuth angle. Its first maximum corresponds to downwind direction, the second in the upwind, and
422 two minima appear in the crosswind direction. Moreover, when speed is lower than 10m/s, the PR
423 presents a linear increase trend with wind speed in the downwind while it is independent on wind
424 speed in other wind directions. Therefore, we fit two PR models which are suitable for large incidence
425 angle using training set. The first is only dependent on incidence angle (Model 1) and the other one
426 adds additional azimuth angle variable (Model 2). The results of two models on the testing set show
427 that the PR models fitted in this paper are superior to models given in previous studies [24-28,45].
428 The Model 2 has higher polarization conversion accuracy than Model 1, with RMSE 0.443dB and
429 correlation coefficient 0.98.

430 6. Conclusion

431 To date, GF-3 satellite only operates for less than two years and is still in the preliminary
432 application stage. Since SAR images before February 2017 lack saturation coefficients and it cannot
433 confirm whether the data is saturated or not, images used in this paper are all collected after March.
434 Furthermore, as shown in the Table 2, the temporal and spatial distribution of SAR images are not
435 uniform. Most data in the experiment is from the east Pacific Ocean near North America in September,
436 October and November. The three-month data is mainly concentrated in the 205 (41.7°). Therefore,
437 the beam 205 is the main part of the data. The collected SAR images whose incidence angles are lower

438 than 39° (lower than beam 200) are concentrated in March and April. They are all saturated and
 439 cannot be used. The reason for this may be inappropriate receiver gain setting at initial period of
 440 satellite operation. These lead to the non-uniformity distribution of incidence angle. In addition, we
 441 use the calibration constants after correction in cross-pol wind retrieval. And the noise floor of QPSI,
 442 QPII and Wave Mode is also slightly different. These may cause that cross-pol retrieval method of
 443 Ren shows a quite different accuracy compared to mine.

444 In the future work, we will collect more Wave Mode images which cover a wide range of
 445 incidence angles and wind speeds in high wind conditions. More system noise gain coefficient files
 446 will also be obtained to analyze the influence of noise floor on cross-pol wind speed retrieval.
 447 Moreover, we will further research the reasons for different polarization ratios under different
 448 operating modes to find a uniform PR model for GF-3 satellite.

449 **Acknowledgments:** The authors thank the National Satellite Ocean Application Service and China Centre for
 450 Resources Satellite Data and Application for providing GF-3 Wave Mode SAR data and calibration constants.
 451 And the wind fields are downloaded from ECMWF EAR-Interim [http://apps.ecmwf.int/datasets/data/interim-
 452 full-daily/levtype=sfc/](http://apps.ecmwf.int/datasets/data/interim-full-daily/levtype=sfc/) for free. We would also like to thank Jingfeng Huang (Zhejiang University) and He Wang
 453 (State Oceanic Administration) for our guidance, and to thank Lanqing Huang (Shanghai Jiao Tong University)
 454 and Lin Ren (State Oceanic Administration) for helpful discussions and suggestions.

455 **Author Contributions:** Lei Wang and Bing Han conceived and performed the experiments. Bin Lei and Chibiao
 456 Ding gave the experimental revisions. Lei Wang drafted the manuscript. And all authors contributed to the
 457 discussion and revising of the manuscript.

458 **Conflicts of Interest:** The authors declare no conflict of interest.

459 Appendix A

460
461

Table 6. Calibration Constants of Oher Beams

beams	constants
202	28.966
203	28.738
206	28.366
207	27.836
208	27.105
209	27.538
210	27.854
211	27.809

462 Appendix B

463
464

Table 7. Index of Abbreviations and Notations

Abbreviations	Full Name
GF-3	Gaofen-3
NOAA	National Oceanic and Atmospheric Administration
SAR	synthetic aperture radar
ECMWF	European Centre for Medium-Range Weather Forecasts
GMFs	empirical geophysical model functions
NRCS	normalized radar cross-section
PR	polarization ratio
NOC	Numerical Ocean Calibration
CAST	China Academy of Space Technology
SLC	single look complex
SNR	signal-to-noise ratio

465
466

467 **References**

- 468 1. Bergeron T, Bernier M, Chokmani K, et al. Wind Speed Estimation Using Polarimetric RADARSAT-2
469 Images: Finding the Best Polarization and Polarization Ratio[J]. IEEE Journal of Selected Topics in Applied
470 Earth Observations & Remote Sensing, 2011, 4(4):896-904.
- 471 2. Zhang B, Perrie W, Vachon P W, et al. Ocean Vector Winds Retrieval From C-Band Fully Polarimetric SAR
472 Measurements[J]. IEEE Transactions on Geoscience & Remote Sensing, 2012, 50(11):4252-4261.
- 473 3. Moon W M, Staples G, Kim D J, et al. RADARSAT-2 and Coastal Applications: Surface Wind, Waterline,
474 and Intertidal Flat Roughness[J]. Proceedings of the IEEE, 2010, 98(5):800-815.
- 475 4. Yang X, Li X, Zheng Q, et al. Comparison of Ocean-Surface Winds Retrieved From QuikSCAT
476 Scatterometer and Radarsat-1 SAR in Offshore Waters of the U.S. West Coast[J]. IEEE Geoscience & Remote
477 Sensing Letters, 2010, 8(1):163-167.
- 478 5. Rivas M B, Stoffelen A, Zadelhoff G J V. The Benefit of HH and VV Polarizations in Retrieving Extreme
479 Wind Speeds for an ASCAT-Type Scatterometer[J]. IEEE Transactions on Geoscience & Remote Sensing,
480 2014, 52(7):4273-4280.
- 481 6. Xu Q, Lin H, Li X, et al. Assessment of an analytical model for sea surface wind speed retrieval from
482 spaceborne SAR[J]. International Journal of Remote Sensing, 2010, 31(4):993-1008.
- 483 7. Horstmann J, Koch W, Lehner S, et al. Wind retrieval over the ocean using synthetic aperture radar with
484 C-band HH polarization[J]. IEEE Transactions on Geoscience & Remote Sensing, 2000, 38(5):2122-2131.
- 485 8. Plant W J. A two-scale model of short wind-generated waves and scatterometry[J]. Journal of Geophysical
486 Research Oceans, 1986, 91(C9):10735-10749.
- 487 9. Romeiser R, Schmidt A, Alpers W. A three-scale composite surface model for the ocean wave-radar
488 modulation transfer function[J]. Journal of Geophysical Research Oceans, 1994, 99(C5):9785-9801.
- 489 10. Romeiser R, Alpers W. An improved composite surface model for the radar backscattering cross section of
490 the ocean surface: 2. Model response to surface roughness variations and the radar imaging of underwater
491 bottom topography[J]. Journal of Geophysical Research Oceans, 1997, 102(C11):25251-25267.
- 492 11. Zou Q, He Y, Perrie W, et al. Wind-Vector Estimation for RADARSAT-1 SAR Images: Validation of Wind-
493 Direction Estimates Based Upon Geometry Diversity[J]. IEEE Geoscience & Remote Sensing Letters, 2007,
494 4(1):176-180.
- 495 12. Escudero B, Diez A, Mart N A, et al. Scatterometer data interpretation: Estimation and validation of the
496 transfer function CMOD4[J]. Journal of Geophysical Research Oceans, 1997, 102(C3):5767-5780.
- 497 13. Quilfen Y, Chapron B, Elfouhaily T, et al. Observation of tropical cyclones by high-resolution scatterometry.
498 J. Geophys. Res. 103(C4), 7767-7786[J]. Journal of Geophysical Research Atmospheres, 1998, 103(C4):7,767-
499 7,786.
- 500 14. Hersbach H, Stoffelen A, Haan S D. An improved C-band scatterometer ocean geophysical model function:
501 CMOD5[J]. Journal of Geophysical Research Oceans, 2007, 112(C3).
- 502 15. Hersbach H. Comparison of C-Band Scatterometer CMOD5.N Equivalent Neutral Winds with ECMWF[J].
503 Journal of Atmospheric & Oceanic Technology, 2010, 27(4):721-736.
- 504 16. Monaldo F M, Thompson D R, Pichel W G, et al. A systematic comparison of QuikSCAT and SAR ocean
505 surface wind speeds[J]. Geoscience & Remote Sensing IEEE Transactions on, 2004, 42(2):283-291.
- 506 17. Monaldo F, Thompson D. Implications of QuikSCAT and RADARSAT wind comparisons for SAR wind
507 speed model functions[C]// Geoscience and Remote Sensing Symposium, 2002. IGARSS '02. 2002 IEEE
508 International. IEEE, 2002:1881-1883 vol.3.
- 509 18. Yang X, Li X, Pichel W G, et al. Comparison of Ocean Surface Winds From ENVISAT ASAR, MetOp ASCAT
510 Scatterometer, Buoy Measurements, and NOGAPS Model[J]. IEEE Transactions on Geoscience & Remote
511 Sensing, 2011, 49(12):4743-4750.
- 512 19. Mouche A A, Hauser D, Daloze J F, et al. Dual-polarization measurements at C-band over the ocean: results
513 from airborne radar observations and comparison with ENVISAT ASAR data[J]. IEEE Transactions on
514 Geoscience & Remote Sensing, 2007, 43(4):753-769.
- 515 20. Rodrigues D F, Landau L, Junior A R T, et al. Sea Wind Extraction From RADARSAT-2 and Scatterometer
516 Data Over the Gulf of Mexico[J]. IEEE Geoscience & Remote Sensing Letters, 2017, 14(7):1007-1011.
- 517 21. Monaldo F M, Thompson D R, Pichel W G, et al. Comparison of RADARSAT SAR-derived wind speeds
518 with buoy and QuikSCAT measurements[C]// Geoscience and Remote Sensing Symposium, 2001. IGARSS
519 '01. IEEE 2001 International. IEEE, 2001:1759-1760 vol.4.

- 520 22. Horstmann J, Koch W, Lehner S, et al. Coastal high-resolution wind fields retrieved from RADARSAT-1
521 ScanSAR[C]// Geoscience and Remote Sensing Symposium, 2001. IGARSS '01. IEEE 2001 International.
522 IEEE, 2001:1747-1749 vol.4.
- 523 23. F. Monaldo, C. Jackson, X. Li, and W. G. Pichel, Preliminary evaluation of Sentinel-1A wind speed
524 retrievals, IEEE [J]. Sel. Topics Appl. Earth Obs. Remote Sens., vol. 9, no. 6, pp. 2638–2642, Jun. 2016.
- 525 24. Thompson, D.R.; Elfouhaily, T.M.; Chapron, B. Polarization ratio for microwave backscattering from the
526 ocean surface at low to moderate incidence angles. In Proceedings of the IEEE International Geoscience
527 and Remote Sensing Symposium, Seattle, WA, USA, 6–10 July 1998; pp. 1671–1673.
- 528 25. Vachon, P.W.; Dobson, F.W. Wind retrieval from RADARSAT SAR images selection of a suitable C-band
529 HH polarization wind retrieval model. Can. J. Remote Sens. 2000, 26, 2122–2131.
- 530 26. Monaldo F M, Thompson D R, Beal R C, et al. Comparison of SAR-derived wind speed with model
531 predictions and ocean buoy measurements[J]. Geoscience & Remote Sensing IEEE Transactions on, 2002,
532 39(12):2587-2600.
- 533 27. Zhang, B.; Perrie, W.G.; He, Y.J. Wind speed retrieval from RADARSAT-2 quad-polarization images using
534 a new polarization ratio model. J. Geophys. Res. 2011, 116, 1318–1323.
- 535 28. Mouche, A.A.; Hauser, D.; Daloze, J.F.; Guerin, C. Dual polarization measurements at C-band over the
536 ocean: Results from airborne radar observations and comparison with ENVISAT ASAR data. IEEE Trans.
537 Geosci. Remote Sens. 2005, 43, 753–769.
- 538 29. Wang H, Yang J, Mouche A, et al. GF-3 SAR Ocean Wind Retrieval: The First View and Preliminary
539 Assessment[J]. Remote Sensing, 2017, 9(7):694.
- 540 30. Hwang P A, Zhang B, Perrie W. Depolarized radar return for breaking wave measurement and hurricane
541 wind retrieval[J]. Geophysical Research Letters, 2010, 37(1):70-75.
- 542 31. Hwang P A, Zhang B, Toporkov J V, et al. Comparison of composite Bragg theory and quad-polarization
543 radar backscatter from RADARSAT-2: With applications to wave breaking and high wind retrieval[J].
544 Journal of Geophysical Research Oceans, 2010, 115(C11):-.
- 545 32. Vachon P W, Wolfe J. C-Band Cross-Polarization Wind Speed Retrieval[J]. IEEE Geoscience & Remote
546 Sensing Letters, 2011, 8(3):456-459.
- 547 33. Zhang B, Perrie W. Cross-Polarized Synthetic Aperture Radar: A New Potential Measurement Technique
548 for Hurricanes[J]. Bulletin of the American Meteorological Society, 2011, 93(4):531-541.
- 549 34. Hwang P A, Perrie W, Zhang B. Cross-Polarization Radar Backscattering From the Ocean Surface and Its
550 Dependence on Wind Velocity[J]. IEEE Geoscience & Remote Sensing Letters, 2014, 11(12):2188-2192.
- 551 35. Hwang P A, Stoffelen A, Zadelhoff G J V, et al. Cross-polarization geophysical model function for C-band
552 radar backscattering from the ocean surface and wind speed retrieval[J]. Journal of Geophysical Research
553 Oceans, 2015, 120(2):893-909.
- 554 36. Shen H, Perrie W, He Y, et al. Wind Speed Retrieval From VH Dual-Polarization RADARSAT-2 SAR
555 Images[J]. IEEE Transactions on Geoscience & Remote Sensing, 2014, 52(9):5820-5826.
- 556 37. Horstmann J, Falchetti S, Wackerman C, et al. Tropical Cyclone Winds Retrieved From C-Band Cross-
557 Polarized Synthetic Aperture Radar[J]. IEEE Transactions on Geoscience & Remote Sensing, 2015,
558 53(5):2887-2898.
- 559 38. Huang L, Liu B, Li X, et al. Technical Evaluation of Sentinel-1 IW Mode Cross-Pol Radar Backscattering
560 from the Ocean Surface in Moderate Wind Condition[J]. Remote Sensing, 2017, 9(8):854.
- 561 39. Horstmann J, Lehner S. A new method for radiometric calibration of spaceborne SAR and its global
562 monitoring[C]// Geoscience and Remote Sensing Symposium, 2002. IGARSS '02. 2002 IEEE International.
563 IEEE, 2002:620-622 vol.1.
- 564 40. Stoffelen A. A Simple Method for Calibration of a Scatterometer over the Ocean[J]. Journal of Atmospheric
565 & Oceanic Technology, 2010, 16(2):275-282.
- 566 41. Verspeek J, Stoffelen A, Verhoef A, et al. Improved ASCAT Wind Retrieval Using NWP Ocean
567 Calibration[J]. IEEE Transactions on Geoscience & Remote Sensing, 2012, 50(7):2488-2494.
- 568 42. Zhu J, Dong X, Yun R. Calibration and validation of the HY-2 scatterometer backscatter measurements over
569 ocean[J]. 2014(IGARSS):4382-4385.
- 570 43. Sun, J.L.; Yu, W.D.; Deng, Y.K. The SAR payload design and performance for the GF-3 mission. Sensors
571 2017,17, 2419
- 572 44. Shao W, Sheng Y, Sun J. Preliminary Assessment of Wind and Wave Retrieval from Chinese Gaofen-3 SAR
573 Imagery.[J]. Sensors, 2017, 17(8).

- 574 45. Ren L, Yang J, Mouche A, et al. Preliminary Analysis of Chinese GF-3 SAR Quad-Polarization
575 Measurements to Extract Winds in Each Polarization[J]. Remote Sensing, 2017, 9(12):1215.
- 576 46. Wang H, Wang J, Yang J et al. Empirical Algorithm for Significant Wave Height Retrieval from Wave Mode
577 Data Provided by the Chinese Satellite Gaofen-3[J]. Remote Sensing, 2018, 10(3), 363.
- 578 47. Shao W, Yuan X, Sheng Y, et al. Development of Wind Speed Retrieval from Cross-Polarization Chinese
579 Gaofen-3 Synthetic Aperture Radar in Typhoons[J]. Sensors, 2018, 18(2).
- 580 48. Chang Y, Li P, Yang J, et al. Polarimetric Calibration and Quality Assessment of the GF-3 Satellite Images[J].
581 Sensors, 2018, 18(2):403.
- 582 49. Horstmann J, Schiller H, Schulz-Stellenfleth J, et al. Global wind speed retrieval from SAR[J]. Geoscience
583 & Remote Sensing IEEE Transactions on, 2003, 41(10):2277-2286.
- 584 50. ECMWF ERA-Interim Daily. Available online: [http://apps.ecmwf.int/datasets/data/interim-full-](http://apps.ecmwf.int/datasets/data/interim-full-daily/levtype=sfc/)
585 [daily/levtype=sfc/](http://apps.ecmwf.int/datasets/data/interim-full-daily/levtype=sfc/)
- 586 51. Birrer I J, Bracalente E M, Dome G J, et al. σ° Signature of the Amazon Rain Forest Obtained from the Seasat
587 Scatterometer[J]. IEEE Transactions on Geoscience & Remote Sensing, 2007, GE-20(1):11-17.
- 588 52. Hawkins R, Attema E, Crapolicchio R, et al. Stability of Amazon Backscatter at C-Band: Spaceborne Results
589 from ERS-1/2 and RADARSAT-1.[J]. 1999, 450:99.
- 590 53. Shao W, Sun J, Guan C, et al. A Method for Sea Surface Wind Field Retrieval from SAR Image Mode Data[J].
591 Journal of Ocean University of China, 2014, 13(2):198-204.
- 592 54. Raney R K, Freeman T, Hawkins R W, et al. A plea for radar brightness[C]// Geoscience and Remote Sensing
593 Symposium, 1994. IGARSS '94. Surface and Atmospheric Remote Sensing: Technologies, Data Analysis and
594 Interpretation. International. IEEE Xplore, 1994:1090-1092 vol.2.
- 595